

A fast and efficient tool to study the rheology of dense suspensions

Cite as: Phys. Fluids **33**, 103314 (2021); <https://doi.org/10.1063/5.0065655>

Submitted: 04 August 2021 • Accepted: 29 September 2021 • Published Online: 12 October 2021

 Alessandro Monti,  Vikram Rathee,  Amy Q. Shen, et al.



View Online



Export Citation



CrossMark

Physics of Fluids

SPECIAL TOPIC: Flow and Acoustics of Unmanned Vehicles

Submit Today!



A fast and efficient tool to study the rheology of dense suspensions

Cite as: Phys. Fluids **33**, 103314 (2021); doi: [10.1063/5.0065655](https://doi.org/10.1063/5.0065655)

Submitted: 4 August 2021 · Accepted: 29 September 2021 ·

Published Online: 12 October 2021



View Online



Export Citation



CrossMark

Alessandro Monti,^{1,a)}  Vikram Rathee,² Amy Q. Shen,²  and Marco E. Rosti^{1,a)} 

AFFILIATIONS

¹Complex Fluids and Flows Unit, Okinawa Institute of Science and Technology, 1919-1 Tancha, Onna, Kunigami District, Okinawa 904-0495, Japan

²Micro/Bio/Nanofluidics Unit, Okinawa Institute of Science and Technology, 1919-1 Tancha, Onna, Kunigami District, Okinawa 904-0495, Japan

^{a)}Authors to whom correspondence should be addressed: alessandro.monti@oist.jp and marco.rosti@oist.jp

ABSTRACT

A cutting-edge software that adopts an optimized searching algorithm is presented to tackle the Newton–Euler equations governing the dynamics of dense suspensions in Newtonian fluids. In particular, we propose an implementation of a fixed-radius near neighbors search based on an efficient counting sort algorithm with an improved symmetric search. The adopted search method drastically reduces the computational cost and allows an efficient parallelization even on a single node through the multi-threading paradigm. Emphasis is also given to the memory efficiency of the code since the history of the contacts among particles has to be traced to model the frictional contributions, when dealing with dense suspensions of rheological interest that consider non-smooth interacting particles. An effective procedure based on an estimate of the maximum number of the smallest particles surrounding the largest one (given the radii distribution) and a sort applied only to the surrounding particles only is implemented, allowing us to effectively tackle the rheology of non-monodispersed particles with a high size-ratio in large domains. Finally, we present validations and verification of the numerical procedure, by comparing with previous simulations and experiments, and present new software capabilities.

© 2021 Author(s). All article content, except where otherwise noted, is licensed under a Creative Commons Attribution (CC BY) license (<http://creativecommons.org/licenses/by/4.0/>). <https://doi.org/10.1063/5.0065655>

I. INTRODUCTION

The physics of granular particles suspended in a fluid has become of fundamental importance in the last few decades due to their heavy involvement in many natural and industrial processes. For instance, clarifying the behavior of blood flows is a high-priority topic since it can potentially lead to the diagnosis and prevention of cardiovascular diseases.¹ From a geophysical viewpoint, phenomena like sediment transport are highly attractive since dense suspensions contribute to transporting nutrients and providing ecological habitats while shaping the surrounding landscape.² Industries working with paints or adhesives, instead, are interested in the control of the flow to guarantee the required performance and quality of the final products approaching the market.³

The physics of the processes listed above is dominated by the interactions between the particles and fluid that determine the flow-ability properties of the granular suspensions. Unscrambling the cumbersome microscopic mechanisms of the interactions between the particles shaping those materials and their flowing behavior has

become a high-priority topic, with a particular need for finding a physically meaningful constitutive law.⁴ Exceptionally challenging is the rheological behavior shown by dense suspensions, i.e., suspensions with a similar volume fraction of particles and liquid. In fact, under stress, dense suspensions may show rheological behaviors that span from a yielded behavior to discontinuous shear-thickening.^{5–8}

Despite the practical relevance, a few analytical studies dealing only with very dilute⁹ and semi-dilute¹⁰ granular suspensions have been successfully carried out. The major mathematical difficulties stand in the lack of proper analytical formulations that deal with multi-body interactions, especially for very large volume fractions, where enduring direct contacts becomes fundamental.⁶ Conversely to theoretical approaches, numerical algorithms are ideal for tackling the numerous particles interacting with each other. Numerical techniques, spanning from molecular dynamics^{11,12} to the solution of the linear Stokes equations for every suspended particle,¹³ stormed the field of granular suspensions. Recently, since the work done in the seminal paper by Cundall and Strack,¹⁴ the discrete (or distinct) element

method (DEM) for studying dense suspensions and granular flows has become the standard for the flow analysis. Modern approaches to DEM reduce the description of the particle–fluid and particle–particle interactions to minimal models able to correctly address the macroscopic behavior of the flow without excessive loss of information. On this fashion, simplified relationships for short-range interactions have been proposed, e.g., for hydrodynamic interactions^{15,16} and for adhesive–repulsive contributions (a satisfactory overview can be found in the works of Refs. 16–19). Concerning contacts, the most implemented technique is the soft-particle model, where contacts among several particles and adhesion effects are handled.¹⁸ In particular, Luding²⁰ developed a minimal model that, based on the original work by Cundall and Strack,¹⁴ addresses the surface roughness of the particles with tangential contacts replicating the sliding, rolling, and torsion resistances, with the option of reproducing both static and dynamic frictions. More advanced contact models contemplating non-linearity, hysteresis, and complex effects can be found in his work.²⁰ Many other models have been adopted in the field of dense suspensions and DEM;^{8,21} the interested reader is referred to the reviews by Li *et al.*¹⁸ and Guo and Curtis²² for a complete overview.

The major drawback of DEM is the expensive computation of short-range interactions acting on every particle. The computational cost, if care is not taken, may quadratically increase with the number of particles considered, limiting the size of the domain analyzable or the length of the simulated process. To reduce the computational cost, algorithms of fixed-radius near neighbors search²³ have been adopted and become the standard in DEM implementations. A widely implemented method is related to the use of Verlet lists.¹² The Verlet list is a data structure that stores and tracks all particles within a cutoff distance of each other. The list can be naively built by checking the $N(N - 1)/2$ distances [cost $O(N^2)$] between particles or, with more modern techniques, through efficient cell-lists or tree-structures that largely reduce the computational cost [$O(N)$ for cell-lists, $O(N \log N)$ for tree structures].²⁴ In particular, the former consists of dividing the computational box into a Cartesian lattice (with spacing Δ that accommodates the particles within a pre-selected cutoff distance) and assigning the particles to the points of the lattice. After that, for each particle a distance-checking procedure is applied to all the other particles belonging to the 27 neighboring cells. This procedure, however, may bring to a high computational and memory cost when dealing with highly polydispersed particles, since the cutoff distance is usually calibrated with the largest particles; therefore, a cell may contain a large number of small particles that must be enquired for neighborhood. While computationally the extra-cost can be decreased by adopting a cutoff radius that suits the smallest particle of the set, and extending the size of the searching-stencil for the larger particles as done in LAMMPS, memory-wise the cost will remain of the order $O(N^2)$, since the cell-list has to spatially cover the whole simulation box.

To further reduce the computational cost, the Verlet-lists are updated every n time steps, calibrated such that within the $n - 1$ remaining steps the locations of the neighboring particles do not significantly vary.¹² This last point, however, is very delicate since updating the Verlet list too frequently is computationally expensive and, on the contrary, increasing the time-period of the update can introduce errors in the computation.

Here, following the work by Hoetzlein,²⁵ we implement a highly parallelisable method based on the cell-list approach that does not

require the explicit computation of a Verlet list, thus zeroing its memory-cost, since the particles will be simply reordered within the Cartesian lattice in a new array by means of a very efficient counting-sort algorithm [computational cost $O(N)$]. Since the particles are ordered by the cell, it is straight-forward to look for neighbors within the adjacent cells. The counting-sort algorithm will be applied to the particles at every time iteration, avoiding any loss of information on the neighboring pairs. Within the framework of this manuscript, we propose and validate the new software that combines the cutting-edge algorithm just mentioned for the neighbors query with methods that satisfactorily deal with complex rheological behaviors observed in dense suspensions. For the latter problem, a rigorous mathematical formulation will be provided. Finally, the software is parallelized within the multi-threading architecture and is intended to be used without accessing the expensive computational power provided by supercomputers or costly Graphics Processing Unit (GPU) accelerators.

The manuscript is organized as follows. Section II deals with the mathematical formulation, focusing on the models adopted and detailing the parameters that govern the flow. In addition, the numerical integration scheme together with its implementation and parallel performance are described. In Sec. III, we show the validation of the code by studying the rheology of dense suspensions to ensure the reliability of the results. Some benchmark tests on the potentiality of the code are also proposed. Finally, in Sec. IV a summary of the code capabilities and novelty ends the manuscript.

II. NUMERICAL METHOD

The in-house software used in this work models a dense, non-Brownian suspension of quasi-inertial, neutrally buoyant, quasi-rigid spherical particles in a shear-flow defined by the shear-rate, $\dot{\gamma}$, and the strain-rate tensor, \mathbb{E}^∞ (with the only non-zero quantities, $\mathbb{E}_{12}^\infty = \mathbb{E}_{21}^\infty = \dot{\gamma}/2$). The code tackles the Newton–Euler equations that govern the translational and rotational dynamics of the rigid particles,

$$\begin{cases} m_i \frac{d\mathbf{u}_i}{dt} = \sum_M \mathbf{F}_i^M, \\ \mathbb{I}_i \frac{d\boldsymbol{\omega}_i}{dt} + \boldsymbol{\omega}_i \times (\mathbb{I}_i \boldsymbol{\omega}_i) = \sum_M \mathbf{T}_i^M, \end{cases} \quad (1)$$

where the subscript i indicates the particle $i \in [1, N]$, N being the number of particles. In Eq. (1), \mathbf{F}_i^M and \mathbf{T}_i^M denote the force and torque applied to the center of mass of the i th particle, with mass m_i and inertia tensor \mathbb{I}_i . The translational and angular velocities are here denoted by the symbols \mathbf{u}_i and $\boldsymbol{\omega}_i$, respectively. The superscript M refers to the nature of the forces applied to system (1), resulting from particle–particle and particle–flow interactions. In particular, here we consider the contributions arisen from hydrodynamics, inelastic contacts, and electro-chemical effects. Specifically, the right-hand-side of Eq. (1) can be written as

$$\begin{cases} \sum_M \mathbf{F}_i^M = \sum_{j=1}^{N_H} \mathbf{F}_{ij}^H + \sum_{j=1}^{N_C} \mathbf{F}_{ij}^C + \sum_{j=1}^{N_E} \mathbf{F}_{ij}^E, \\ \sum_M \mathbf{T}_i^M = \sum_{j=1}^{N_H} \mathbf{T}_{ij}^H + \sum_{j=1}^{N_C} \mathbf{T}_{ij}^C + \sum_{j=1}^{N_E} \mathbf{T}_{ij}^E, \end{cases} \quad (2)$$

where the summations are performed on the number of particles neighboring the i th particle considered, and the superscripts H , C , and E stand for hydrodynamics, inelastic contacts, and electro-chemical effects, respectively.

Concerning the hydrodynamics of the system, dense suspensions of rigid particles immersed in a low-Reynolds-number flow are subjected to a Stokes drag and a pair-wise, short-range lubrication force.²⁶ The latter is caused by the relative motion of particles that squeeze the fluid flowing in the narrow gaps between them. Following the work of Ball and Melrose¹⁵ and Mari *et al.*,²⁶ to replicate those contributions we implement a linear relationship between forces and velocities,

$$\begin{pmatrix} \mathbf{F}_i^H \\ \mathbf{F}_j^H \\ \mathbf{T}_i^H \\ \mathbf{T}_j^H \end{pmatrix} = -(\mathbb{R}_{Stokes} + \mathbb{R}_{Lub})_{ij} \cdot \begin{pmatrix} \mathbf{u}_i - \mathbf{U}^\infty(\mathbf{x}_i) \\ \mathbf{u}_j - \mathbf{U}^\infty(\mathbf{x}_j) \\ \boldsymbol{\omega}_i - \boldsymbol{\Omega}^\infty(\mathbf{x}_i) \\ \boldsymbol{\omega}_j - \boldsymbol{\Omega}^\infty(\mathbf{x}_j) \end{pmatrix} + (\mathbb{R}'_{Lub}(\mathbb{E}))_{ij} \begin{pmatrix} \mathbf{n} \\ \mathbf{n} \\ \mathbf{n}_{\perp,i} \\ \mathbf{n}_{\perp,j} \end{pmatrix}, \quad (3)$$

where $\mathbf{n} = (\mathbf{x}_j - \mathbf{x}_i)/|\mathbf{x}_j - \mathbf{x}_i|$ is the center-to-center unit vector (being \mathbf{x}_i the Cartesian position of the particle i), and $\mathbf{n}_{\perp,i}(A) = 2\mathbf{n} \times [(A_i + A_j^T) \cdot \mathbf{n}]$ is a vector perpendicular to \mathbf{n} (being A_i the strain-rate tensor referred to the i th particle, \mathbb{E}_i^∞ , in this case), \mathbb{R}_{Stokes} is a diagonal matrix that models the Stokes drag forces and torques, including the Faxén laws for non-uniform shear-flows,²⁷ and \mathbb{R}_{Lub} and \mathbb{R}'_{Lub} are sparse matrices that approximate the far-field mobility matrices, dropping the low moment contributions and considering a pair resistance model with only divergent terms.¹⁵ In particular, those sparse matrices model the contribution of the lubrication through the squeeze, shear, and pump modes.²⁶ The detailed formulation of the matrices defining the hydrodynamics resistances is given in A. Figure 1 sketches the lubrication forces and torques acting on the i th particle (left) due to the presence of the j th particle (right). The dashed red circumference highlights the region of influence of the lubricant

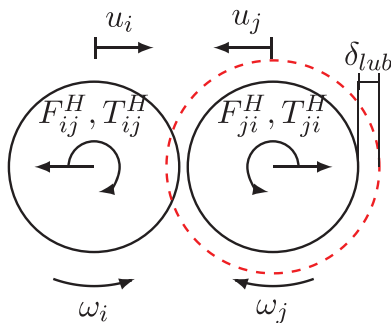


FIG. 1. Sketch of the hydrodynamic interaction between the pair of particles, i, j , having velocity and angular velocity $\mathbf{u}_i, \mathbf{u}_j$ and $\boldsymbol{\omega}_i, \boldsymbol{\omega}_j$, respectively. The hydrodynamics effect starts acting when the minimum surface distance between the particles is below δ_{lub} .

interactions, parameterized with δ_{lub} . Note that beyond this threshold, i.e., even at mid-range distances between the particles, the hydrodynamics is modeled only through the Stokes drag. We acknowledge that this is an approximation; however in the context of dense suspensions, it is acceptable since its contribution is minimal.

The contact contribution is modeled by the stick-and-slide method²⁰ that is able to describe frictional contacts. This method mimics the inelastic contacts with spring-dashpot systems that start operating when the surface distance between the spheres i and j , $d_{ij} = |\mathbf{x}_i - \mathbf{x}_j| - (a_i + a_j)$ (being a_i and a_j the particles radii), is negative (overlap). Considering two particles, i and j , the stick-and-slide model can be written as

$$\mathbf{F}_{ij}^{C,nor} = k_n d_{ij} \mathbf{n} + \gamma_n \mathbf{u}_{n,ij}, \quad (4a)$$

$$\mathbf{F}_{ij}^{C,tan} = k_t \boldsymbol{\xi}_{ij}, \quad (4b)$$

$$\mathbf{F}_{ji}^C = -\mathbf{F}_{ij}^C, \quad (4c)$$

$$\mathbf{T}_{ij}^C = a_i \mathbf{n} \times \mathbf{F}_{ij}^{C,tan}, \quad (4d)$$

$$\mathbf{T}_{ji}^C = (a_j/a_i) \mathbf{T}_{ij}^C, \quad (4e)$$

where the Coulomb's law $|\mathbf{F}_{ij}^{C,tan}| \leq \mu_C |\mathbf{F}_{ij}^{C,nor}|$ must be satisfied (μ_C being the friction coefficient). The superscripts *nor* and *tan* indicate the directions of the force (i.e., normal and tangential) and the parameters k_n, k_t , and γ_n are the normal and tangential spring constants and the normal damping constant, respectively. The velocity $\mathbf{u}_{n,ij} = \mathbf{n} \otimes \mathbf{n} \cdot (\mathbf{u}_j - \mathbf{u}_i)$ is the normal velocity vector, while $\boldsymbol{\xi}_{ij}$ represents the stretch of the tangential spring. The latter is computed following the procedure described by Luding:²⁰

$$\boldsymbol{\xi}_{ij} = \begin{cases} \mathbb{T} \int_{t_0}^t \mathbf{u}_{t,ij} d\tau, & \text{if } |\boldsymbol{\xi}_{ij}| < \frac{\mu_C |\mathbf{F}_{ij}^{C,nor}|}{k_t}, \\ \frac{\mu_C |\mathbf{F}_{ij}^{C,nor}|}{k_t} \frac{\boldsymbol{\xi}_{ij}}{|\boldsymbol{\xi}_{ij}|}, & \text{otherwise,} \end{cases} \quad (5)$$

where $\mathbb{T} = \mathbb{I} - \mathbf{n} \otimes \mathbf{n}$ is the tangential projection tensor, $\mathbf{u}_{t,ij} = \mathbb{T} \cdot (\mathbf{u}_j - \mathbf{u}_i - (a_i \boldsymbol{\omega}_i + a_j \boldsymbol{\omega}_j) \times \mathbf{n})$ is the tangential velocity vector, and t_0 is the time at the beginning of the collision between the particles i and j [with $\boldsymbol{\xi}_{ij}(t_0) = \mathbf{0}$]. A sketch of the model adopted in this work is shown in Fig. 2. The possibility of adding the rolling resistance to the model, as in Refs. 19 and 20, is described in B.

The last contribution considered in this work is forces of conservative nature that arise from the chemo-physical properties of the solid-fluid and solid-solid interactions and play a fundamental role in systems of dense suspensions.^{19,28} In particular, the model, sketched in Fig. 3, addresses the contribution by adding an inter-particle, distance-decaying repulsion force,

$$\mathbf{F}_{ij}^R = \begin{cases} -F_{ER} \frac{\bar{a}}{a_0}, e^{-d_{ij}/\lambda_D} \mathbf{n}, & \text{if } d_{ij} \geq 0, \\ -F_{ER} \frac{\bar{a}}{a_0} \mathbf{n}, & \text{if } d_{ij} < 0, \end{cases} \quad (6a)$$

$$\mathbf{F}_{ji}^R = -\mathbf{F}_{ij}^R, \quad (6b)$$

and an attraction force in van der Waals form,

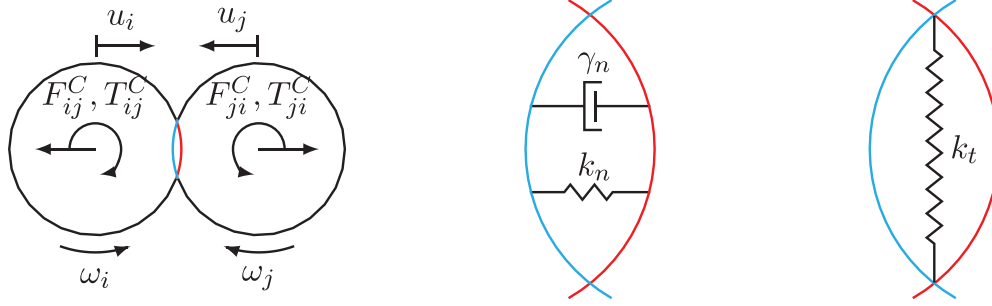


FIG. 2. Sketch of the contacts model between the pair of particles, i, j , having velocity and angular velocity u_i, u_j and ω_i, ω_j , respectively. The spring-dashpot systems modeling the contacts start acting when the surface distance, d_{ij} , between the particles is negative (overlap).

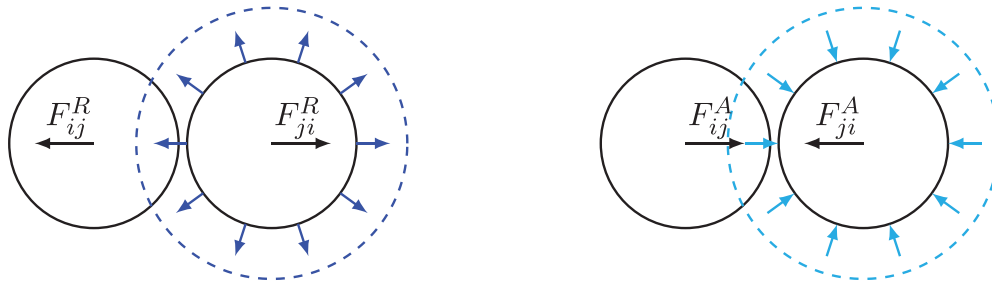


FIG. 3. Sketch of the model adopted for the electro-chemical interaction between the pair of particles, i, j . The repulsive interaction starts appearing when the minimum surface distance between the particles is below $20\lambda_D$, while the attractive contribution when the minimum surface distance is below $4a_0$.

$$F_{ij}^A = \begin{cases} \frac{A\bar{a}}{12(d_{ij}^2 + \epsilon^2)} \mathbf{n}, & \text{if } d_{ij} \geq 0, \\ \frac{A\bar{a}}{12\epsilon^2} \mathbf{n}, & \text{if } d_{ij} < 0. \end{cases} \quad (7a)$$

$$F_{ji}^A = -F_{ij}^A. \quad (7b)$$

In Eq. (6), F_{ER} is the module of the force, a_0 the reference radius, $\bar{a} = 2a_i a_j / (a_i + a_j)$ the harmonic radius, and λ_D is the Debye length that controls the decay of the force. In Eq. (7), instead, A is the Hamaker constant and ϵ is a small regularization term (generally $\epsilon \approx 0.01\bar{a}$) introduced to avoid the singularity at contact, when $d_{ij} = 0$. To simplify the notation, below the repulsive and attractive effects may be gathered together in the electro-chemical contribution, $F^E = F^R + F^A$, marked by the E superscript.

The forcing contributions described above induce mechanical stress in the suspension that can be computed using the stresslets theory,²⁷

$$\Sigma = 2\eta_0 \mathbb{E}^\infty + \frac{1}{V} \sum_{i=1}^N \left(\sum_{j=1}^{N_H} S_{ij}^H + \sum_{j=1}^{N_C} S_{ij}^C + \sum_{j=1}^{N_E} S_{ij}^E \right), \quad (8)$$

where Σ is the bulk stress tensor, η_0 is the viscosity of the carrier fluid, and V is the volume of the simulated box. The stresslets due to the interactions, instead, are denoted by S and are defined as

$$S_i^S = 20/3\pi\eta_0 a_i^3 (1 + a_i^2/10\nabla^2) \mathbb{E}_i^\infty, \quad (9a)$$

$$S_{ij}^L = 0.5 [(\mathbf{x}_j - \mathbf{x}_i) \otimes \mathbf{F}_{ij}^H + ((\mathbf{x}_j - \mathbf{x}_i) \otimes \mathbf{F}_{ij}^H)^T], \quad (9b)$$

$$S_{ij}^C = (\mathbf{x}_j - \mathbf{x}_i) \otimes \mathbf{F}_{ij}^C, \quad (9c)$$

$$S_{ij}^E = (\mathbf{x}_j - \mathbf{x}_i) \otimes \mathbf{F}_{ij}^E, \quad (9d)$$

where the hydrodynamic contribution (H) has been separated into the Stokes (S) and lubrication (L) terms, i.e., $S_{ij}^H = S_i^S + S_{ij}^L$. From the bulk stress tensor, Σ , we can derive the quantities of rheological interest, i.e., the shear-stress σ , the normal stress differences N_1 and N_2 , and the pressure Π , defined as $\sigma = \Sigma_{12}$, $N_1 = \Sigma_{11} - \Sigma_{22}$, $N_2 = \Sigma_{22} - \Sigma_{33}$, and $\Pi = -Tr(\Sigma)/3$. Normalizing the shear-stress and the pressure with the properties of the carrier flow, we can define the relative viscosity and the dimensionless pressure as $\eta_r = \sigma/(\eta_0\dot{\gamma})$ and $\eta_n = \Pi/(\eta_0\dot{\gamma})$, respectively.

Several parameters dominate the physics of the suspension described by System (1). We consider the translational equation of (1),

$$\frac{\rho a_0^3 U}{T} \frac{d\mathbf{u}_i^*}{dt^*} = \eta_0 a_0 U \sum_{j=1}^{N_H} \mathbf{F}_{ij}^{H,*} + k_{eq} a_0 \sum_{j=1}^{N_C} \mathbf{F}_{ij}^{C,*} + F \sum_{j=1}^{N_E} \mathbf{F}_{ij}^{E,*}, \quad (10)$$

where we gathered the dimensional quantities (being the non-dimensional quantities marked with the superscript $*$). In Eq. (10), $U = a_0\dot{\gamma}$ is the typical velocity in a shear-flow, T is the timescale introduced by the particles (in this case, the particles introduce no additional time-scales, therefore $T = 1/\dot{\gamma}$), k_{eq} is the equivalent spring constant of the model represented in Fig. 2, and F is the module of the force introduced by the electro-chemical interactions. Applying the Buckingham Pi theorem, the parameters are reduced to a set of non-dimensional numbers that can be tuned to outline the model desired. Considering the dimensional quantities in Eq. (10), $\{\rho, a_0, \eta_0, \dot{\gamma}, k_{eq}, F\}$ and

choosing $\{a_0, \eta_0, \dot{\gamma}\}$ as independent fundamental quantities, three non-dimensional groups emerge. The first one is the Stokes number,

$$St = \frac{\rho a_0^2 \dot{\gamma}}{\eta_0} \ll 1, \tag{11}$$

where the constraint $St \ll 1$ is applied to remain in the inertialess regime. The non-dimensional stiffness, instead, governs the importance of the contacts contributions compared to the hydrodynamic term,

$$\hat{k} = \frac{k_n}{\eta_0 a_0 \dot{\gamma}} \gg 1, \tag{12}$$

where $\hat{k} \gg 1$ forces the particles to be rigid; note that, the equivalent stiffness constant,

$$k_{eq} = k_n \left(1 + \frac{k_t}{k_n} + \frac{\gamma_n \dot{\gamma}}{k_n} \right), \tag{13}$$

has been approximated to k_n by adding additional constraints $k_t \ll k_n$ and $\gamma_n \dot{\gamma} / k_n \ll 1$.²⁶ Finally, the last non-dimensional group (the equivalent shear-rate) refers to the timescale introduced by the electrochemical contribution,

$$\hat{\dot{\gamma}} = \frac{F(d_{ij} = 0)}{\eta_0 a_0^2 \dot{\gamma}} = \frac{\dot{\gamma}_0}{\dot{\gamma}}, \tag{14}$$

where we defined a new shear-rate, $\dot{\gamma}_0 = F(d_{ij}) / \eta_0 a_0^2$; thus, tuning F (i.e., adjusting F_{ER} and the Hamaker constant) appropriately, a shear-rate dependency can be imposed to the suspension.

A. Numerical algorithm

Following the work by Ge *et al.*,^{29,30} the governing equations (1) are advanced in time with the modified velocity-Verlet explicit scheme,³¹

$$\mathbf{x}_i^{(n+1)} = \mathbf{x}_i^{(n)} + \Delta t \mathbf{u}_i^{(n)} + \frac{\Delta t^2}{2} \boldsymbol{\alpha}_i^{(n)}, \tag{15a}$$

$$\mathbf{u}_i^{(n+1/2)} = \mathbf{u}_i^{(n)} + \frac{\Delta t}{2} \boldsymbol{\alpha}_i^{(n)}, \tag{15b}$$

$$\boldsymbol{\alpha}_i^{n+1} = \mathcal{F}(\mathbf{x}_i^{(n+1)}, \mathbf{u}_i^{(n+1/2)}), \tag{15c}$$

$$\mathbf{u}_i^{(n+1)} = \mathbf{u}_i^{(n)} + \frac{\Delta t}{2} (\boldsymbol{\alpha}_i^{(n)} + \boldsymbol{\alpha}_i^{(n+1)}), \tag{15d}$$

where $\mathbf{x}_i^{(n)}$, $\mathbf{u}_i^{(n)}$, and $\boldsymbol{\alpha}_i^{(n)}$ denote the position (orientation), velocity (angular velocity), and acceleration (angular acceleration) vectors of the particle i , respectively, at time $t = n\Delta t$, and \mathcal{F} resembles the right hand side of Eq. (1). The modified velocity-Verlet scheme is second-order accurate in time and, being explicit, it requires a time step Δt that resolves the smallest timescale of the system (typically established by the stiffness of the contacts; a good approximation of the time step can be computed through the time constant that can be defined in the normal spring-dashpot system, $\Delta t \dot{\gamma} = \gamma_n \dot{\gamma} / k_n$). Different from other approaches, e.g., considering an over-damped system dropping the inertial terms,²⁶ this approach allows us to avoid the inversion of the resistance matrix of the lubrication forces.

The domain is a box of size $L_x \times L_y \times L_z$ (or L^3 if cubic) with a shear-rate, $\dot{\gamma}$, applied along the y direction. At the edges of the domain, the Lees-Edwards boundary conditions³² are adopted to remove the effect of the walls,

$$x = \begin{cases} (x + L_x - \dot{\gamma} L_y t) \bmod L_x, & \text{if } y > L_y, \\ (x + L_x + \dot{\gamma} L_y t) \bmod L_x, & \text{if } y < 0, \\ (x + L_x) \bmod L_x, & \text{otherwise,} \end{cases} \tag{16a}$$

$$y = (y + L_y) \bmod L_y, \tag{16b}$$

$$z = (z + L_z) \bmod L_z, \tag{16c}$$

$$\mathbf{u} = \begin{cases} (\mathbf{u} - \dot{\gamma} t), & \text{if } y > L_y, \\ (\mathbf{u} + \dot{\gamma} t), & \text{if } y < 0. \end{cases} \tag{16d}$$

The interaction between the particles represents the most expensive part of the algorithm from a computational point of view with a cost of $O(N^2)$, if a brute force algorithm is used. To overcome the problem, we adopted a highly parallelisable, fixed-radius near neighbors algorithm.^{23,25} The algorithm is based on rearranging the particles on a coarser lattice (cell-list) by adopting an efficient counting sort algorithm²⁵ that requires a computational cost $O(N)$ and few memory arrays of size N . The spacing of the cell-list Δ must suit the desired searching distance; a sketch of it is shown in Fig. 4. By considering the near points of the coarser grid in the search for neighbors, i.e., the blue-filled region in Fig. 4 (considering a 3×3 macro searching-cell) the computational cost dramatically decreases to $O(cN)$, where $c \ll N$ is the number of particles inquired as neighbors and depends on the lattice space Δ . The dependence of c on Δ is related to the number of particles that fit each macro-cell and an optimal choice of Δ is therefore related to the properties of the suspension. For instance, fixing $\Delta = 2a_{max}$, where a_{max} is the radius of the largest particle in the suspension, minimizes the number of macro-cells to be inquired for the search of neighbors. This is ideal for monodisperse suspensions where there may be at maximum one particle per cell and may look reasonable when considering polydispersed suspensions with not-very-high dispersion ratios. On the contrary, the choice may be detrimental for suspensions with $a_{min} \ll a_{max}$ (a_{min} being the radius of the smallest particle), since it may result in the presence of a high number of particles within each macro-cell, with the limit of $c = N$ when $2a_{max}$ corresponds to the size of the domain. In this case, to reduce the number of particles within each searching cell, a better choice is to set $\Delta < 2a_{max}$ and increase the stencil of neighboring cells.^{24,25}

As a drawback, the search shown in Fig. 4 implies that the forces and torques acting on the pair of particles (i, j) are computed twice, although this procedure guarantees a better load balance through the processes when the code is parallelized. To avoid the double counting of the forces keeping a good load distribution among the processes, we propose a symmetric search, where the neighbors are scanned only over half of the points of the macro searching-cell of the near Cartesian lattice, as sketched in Fig. 5, thus obtaining an additional significant speed-up by halving the computational operations. Note that this procedure does not require any particular symmetry of the problem.

Memory-wise, instead, the main problem arises from the computation of the tangential stretch, Eq. (5), where the history of all contacts must be traced, with a potential memory cost $O(N^2)$. To reduce the cost, we use a reduced matrix with size $N \times M$, where M is an

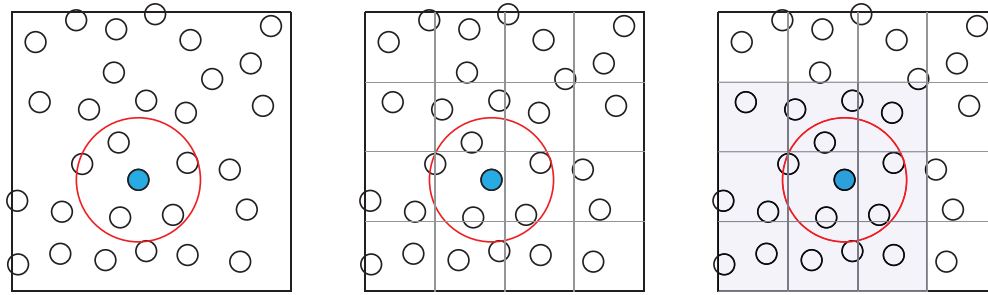


FIG. 4. Sketch of the fixed-radius near-neighbors algorithm adopted for finding the neighbors of the particle highlighted in blue, within a distance R marked by the red circle. The domain (left panel) is subdivided, first, into a coarse lattice (central panel) and the particles are ordered via a counting sort algorithm. The search is then carried out only on the 3×3 neighboring cells (blue region, right panel).

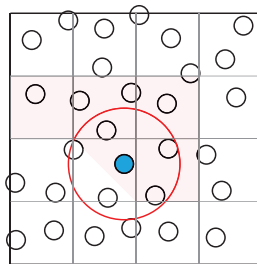


FIG. 5. Symmetric fixed-radius near-neighbors algorithm. The search is carried out only within the red region. The initial random distribution of particles within the domain guarantees the load-balance in the case of parallelization.

overestimation of the maximum number of contacts per particle based on the volume of the spherical shell surrounding the largest particle of the suspension, with thickness $\Delta a = 2a_0$. The contacts, once established, are then recorded into a hash-map that charts them along with the indexes of the particles involved. Then, every array of the map

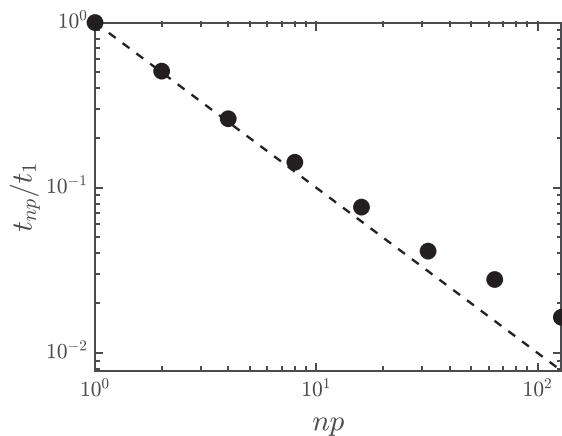


FIG. 6. Scalability of the code. We considered a bidispersed suspension with number of particles $N = 65\,536$ and volume fraction $\phi = 0.5$. The bidispersity of suspension is characterized by a bidispersion ratio $a_2/a_1 = 3$ and volume ratio $V_2/V_1 = 0.25$. The graph is obtained by increasing the number of processes np . The time spent per iteration by np processes, t_{np} , is normalized by the time spent by a single process, t_1 .

(i, M) is sorted by the indexes, and the history of the contacts for the particle i is sought over the sorted array (i, M). This procedure has an actual memory cost $O(N)$, adding little to the computational cost.

The parallelization of the solver is reached by implementing the multi-threading paradigm on a single node with a multiprocessing system, using the OpenMP directives. The high-scalability of the code, obtained on a 2-socket AMD EPYC 7702 machine (zen2 microarchitecture), is shown in Fig. 6. The scalability graph is obtained by fixing the domain properties and varying the number of processes used. The case considered is a bidispersed suspension with a high number of particles $N = 65\,536$ to test also the memory-efficiency, volume fraction $\phi = 0.5$, bidispersity ratio, and volume $a_2/a_1 = 3$ and $V_2/V_1 = 0.25$, respectively. All the forcing contributions listed above in this section have been considered. Referring to the configurations shown in Fig. 6, the total time per iteration (on average) in seconds is reported in Table I. The table also shows the breakdown (in percentage) of the total time needed by the several parts sampled within the core of the software. In particular, t_1 corresponds to the time needed to update the kinematical properties of the particles with the modified velocity-Verlet scheme, t_2 to sort the particles within the corresponding cells (counting sort), t_3 to compute the interactions between neighbors, and t_4 to sort the hash-map of the frictional contacts list, while the amount of time needed for writing the outputs is negligible. The breakdown of the total time per iteration shows how the counting sort algorithm is convenient for reordering the particles within the searching cells, with

TABLE I. List of the average time per iteration needed to advance the particles varying the number of threads and its breakdown. In particular, t_{tot} is the total time in seconds per iteration, t_1 is the percentage of time taken by the modified velocity-Verlet scheme, t_2 is the percentage of time needed to sort the particles within the macro-cells (counting sort), t_3 is the percentage of time needed to compute the interactions between neighboring particles, and t_4 is the percentage of time needed for sorting the hash-map of the lists for the history of the frictional contacts.

np	1	2	4	8	16	32	64	128
t_{tot} (s/iter)	0.549	0.279	0.144	0.078	0.042	0.023	0.015	0.009
t_1 (%)	0.8	0.8	1.0	2.1	2.9	5.5	8.5	8.6
t_2 (%)	0.2	0.4	0.5	1.1	1.4	2.1	3.2	5.7
t_3 (%)	92.4	92.5	91.8	88.0	85.2	79.0	69.7	70.1
t_4 (%)	6.6	6.3	6.7	8.8	10.5	13.4	18.6	15.6

TABLE II. Parameter choice for the frictionless (FL) and frictional (FR) configurations. Here, $a_0 = a_1$ represents the reference length scale.

	N	a_2/a_1	V_2/V_1	St	\hat{k}	k_t/k_n	$\gamma_n \dot{\gamma}/k_n$	μ_C	$\dot{\gamma}/\dot{\gamma}_0$	δ_{lub}/a_0
FL	200	1.4	1	10^{-3}	4×10^5	2/7	10^{-7}	0	∞	{0.05, 0.2}
FR	1000	1.4	1	10^{-3}	4×10^5	2/7	10^{-7}	1	∞	{0.05, 0.2}

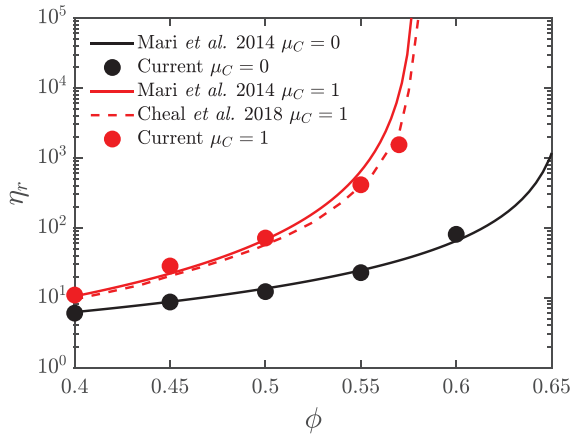


FIG. 7. Relative viscosity, η_r (filled markers), varying the volume fraction. The solid curves represents the power-law fitting of the data from Ref. 26. The black solid curve, $\eta_r = 1.4(1 - \phi/\phi_J)^{-1.6}$, with jamming volume fraction $\phi_J = 0.66$, is obtained for frictionless particles, while the red solid curve, $\eta_r = 0.71(1 - \phi/\phi_J)^{-2.3}$, with jamming volume fraction $\phi_J = 0.575$, is obtained for frictional particles with $\mu_C = 1$. The red dashed line, instead, is obtained from the numerical data by Cheal and Ness³⁴ for frictional particles with $\mu_C = 1$.

its cost not exceeding the 6% of the total time in the configuration considered.

For readers interested in the algorithm and in benchmarking the software, the code is available at <https://github.com/marco-rosti/CFB-Ball-0x>.

III. RESULTS

In this section, the robustness and accuracy of the method proposed above for dense suspensions is investigated. We consider, first, a relatively small domain with particles suspended in a uniform, plain shear-flow, and we compare the data obtained with studies available in the literature varying the volume fraction and the shear-rate; we then increase the domain size to test the memory-efficiency of the software, and we study the behavior of a dense suspension subject to a wavy shear-flow, the wave acting on the stream-shear cross-plane. All initial

conditions used in this work are generated with the sphere-packing software developed by Donev.³³

A. Uniform shear-flow

The reliability of the code has been tested both in jamming transition scenarios and in a shear-dependent behavior of rheological relevance.

For the jamming transition, we consider a cubic box containing a bidispersed suspension ($a_2/a_1 = 1.4$, in equal volumes $V_2/V_1 = 1$) of 200 frictionless, rigid [see Eq. (12)] particles, with no electro-chemical interactions. The side length of the box accommodates the volume fraction ϕ imposed, being $a_0 = a_1 = 1$. The parameters chosen echo the validation carried out by Ge and Brandt²⁹ and are listed in Table II. Figure 7 shows the comparison between the simulation results and the data available in the literature with a satisfying agreement between the computed relative viscosity, η_r , and the power-law fitting of Mari *et al.*²⁶ for frictionless particles (solid black curve).

We then activate the friction ($\mu_C = 1$), and we increase the number of particles to $N = 1000$ (see Table II). Figure 7 shows the comparison between the computed relative viscosity η_r and the data fitting obtained by Mari *et al.*²⁶ (solid red curve) and Cheal and Ness³⁴ (dashed red curve) with excellent agreement.

The shear-dependent behavior of the particles suspended in a uniform shear-flow is obtained by considering all contributions listed in Sec. II. At first, we will show the results obtained from a bidispersed dense suspensions (size ratio $a_2/a_1 = 1.4$) with volume fraction $\phi = [0.45, 0.50, 0.55]$, to see if the software is able to catch the typical shear-dependent behavior.²⁶ The set of parameters for carrying out these simulations have been chosen to mimic those by Mari *et al.*²⁶ and are listed in Table III. Note that for these simulations, the electro-chemical contribution is purely repulsive ($F_R/F_A = \infty$), as set in Mari *et al.*²⁶ Figure 8 (left panel) shows the trend of the relative viscosity η_r , varying the shear-rate applied to the suspension $\dot{\gamma}/\dot{\gamma}_0$. In particular, we see that the three suspensions show the same qualitative behavior, with values of the relative viscosity substantially increasing (especially at higher shear-rates) with the volume fraction. From Fig. 8, we can notice that at low shear-rates the suspensions show the typical shear-thinning behavior with a similar slope in the three cases considered, as already observed by Mari *et al.*²⁶ At those shear-rates, the repulsive

TABLE III. Set of parameters used for simulating the behavior of dense suspensions varying the shear rate. Here, $a_0 = a_1$ is the reference length scale.

ϕ	N	a_2/a_1	V_2/V_1	St	\hat{k}	k_t/k_n	$\gamma_n \dot{\gamma}/k_n$	μ_C	$\dot{\gamma}/\dot{\gamma}_0$	δ_{lub}/a_0	λ_D/a_0	F^R/F^A
0.45	512	1.4	1	10^{-3}	4×10^5	2/7	10^{-7}	1.0	{ $10^{-5}, \dots, 10$ }	0.10	0.05	∞
0.50	512	1.4	1	10^{-3}	4×10^5	2/7	10^{-7}	1.0	{ $10^{-5}, \dots, 10$ }	0.10	0.05	∞
0.55	512	1.4	1	10^{-3}	8×10^5	2/7	10^{-7}	1.0	{ $10^{-5}, \dots, 10$ }	0.10	0.05	∞

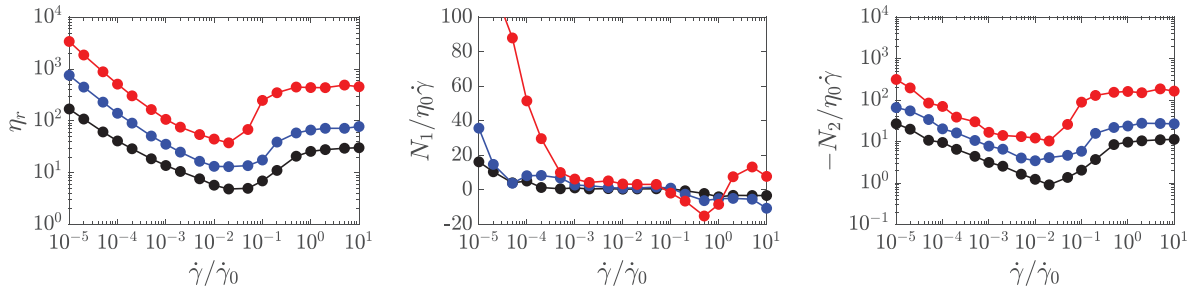


FIG. 8. Shear-dependent rheological quantities of dense suspensions with $\phi = [0.45, 0.50, 0.55]$, indicated by the black, blue and red lines, respectively. Left panel: relative viscosity, η_r ; middle panel: first normal stress difference N_1 normalized with the shear stress of the carrier fluid; right panel: Second normal stress difference N_2 normalized with the shear stress of the carrier fluid.

TABLE IV. Parameters set used for numerical simulations (SI) and experiments (EX) of particles suspended in a varying uniform shear-flow. Here, a_0 ($= a_1$ in the simulations) stands for the reference length scale.

	N	a_2/a_1	V_2/V_1	St	\hat{k}	k_t/k_n	$\gamma_n \dot{\gamma}/k_n$	μ_C	$\dot{\gamma}/\dot{\gamma}_0$	δ_{lub}/a_0	λ_D/a_0	F^R/F^A
SI	512	1.09	1	10^{-3}	4×10^5	2/7	10^{-7}	0.5	$\{10^{-5}, \dots, 10\}$	0.25	[0.0225, 0.0065]	[19, 1]
EX		a_0		η_0			ρ_{fluid}	μ_C			λ_D	$NaCl$
		208 ± 5 nm		0.108 Pa s			1.12 g/cm ³	0.5			[4.5, 1] nm	[0.4, 0] M

contribution dominates the mechanics of the suspensions (higher F^E , lower $\dot{\gamma}/\dot{\gamma}_0$), holding the particles off at a mid-range distance. On the other hand, at higher shear-rates the contacts become dominant, triggering the typical shear-thickening behavior, with a growing slope as the volume fraction is increased, eventually leading to a quasi-discontinuous shear-thickening at $\phi = 0.55$. When considering dense suspensions, to characterize the strain-induced anisotropy of the fluid, two additional rheologically meaningful functions are usually measured: the two independent normal stress differences N_1 and N_2 . Fig. 8 shows the first (middle panel) and the second (right panel) normal stress differences, respectively, of the shear-dependent suspensions considered (see Table III). In particular, the trend observed is similar to the one reported by Mari *et al.*,²⁶ proving the capability of the software to catch the strain-induced anisotropies of the suspensions.

Next, we consider a dense suspension with volume fraction $\phi = 0.46$, and we compare our numerical results with experimental data obtained from quasi-neutrally buoyant silica colloidal particles, processed through the Stöber method,^{35,36} suspended in a glycerol–water solution with relative concentration 80% – 20%, respectively. The electro-chemical properties of the suspension were altered by adding sodium-chloride (NaCl) to the solution, as done in Rathee *et al.*³⁷ In particular, the numerical and experimental parameters are reported in Table IV. Figure 9 shows a very good agreement between the relative viscosity, η_r , obtained from the numerical and experimental data, for both salt concentrations considered. For the experimental results, the shear-rate $\dot{\gamma}$ has been normalized to match the domain span of the numerical data. The two suspensions behave very differently at lower shear-rates, i.e., in the shear-thinning region. In that regime, the electro-chemical potential acting on the suspension dominates its mechanics. Increasing the salt concentration, the electro-chemical properties of the suspension are modified, with the contribution due to the van der Waals attractive forces becoming more important (lower F_R/F_A). This induces the

formation of large clusters that highly contribute to the higher resistance of the suspension to flow,³⁷ and this is reflected in Fig. 9, with the red curve showing much higher values of η_r . Conversely, at higher shear-rates, where the contacts between particles dominate, the behavior of the suspension does not depend on the salt concentration; therefore, the two suspensions have similar values of relative viscosities (see Fig. 9).³⁷

The typical size of the cluster of particles for the suspension with higher salt concentration is shown in Fig. 10. In particular, the two panels show the size distribution of the clusters at the extrema of the curve in Fig. 9, i.e., at shear-rate $\dot{\gamma}/\dot{\gamma}_0 = [10^{-5}, 10^0]$, when the

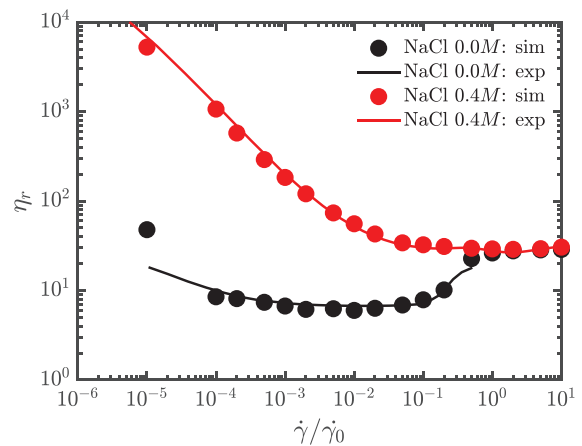


FIG. 9. Relative viscosity, η_r , varying the shear-rate, $\dot{\gamma}/\dot{\gamma}_0$, where for the experiments, the value $\dot{\gamma}_0$ has been chosen to match the shear-rate domain of the simulations. The symbols outline the numerical data, while the solid lines represent the experimental results. The black data are obtained from a salt-free suspension, while the red data represent the solution with salt concentration 0.4M.

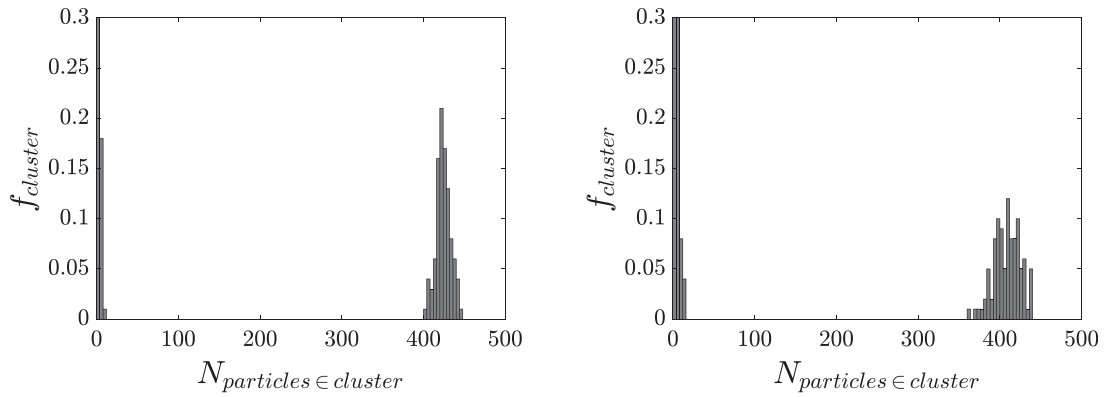


FIG. 10. Average size distribution of clusters of contacting particles for the strongly attractive suspension (i.e., salt concentration $0.4M$). Left panel: $\dot{\gamma}/\dot{\gamma}_0 = 10^{-5}$; right panel: $\dot{\gamma}/\dot{\gamma}_0 = 10^0$. The total number of particles is $N = 512$. The size distributions are averaged over 100 snapshots.

suspension reaches its steady-state regime. From Fig. 10, we can see that the distributions show two peaks, the leftmost one concerning small clusters and the rightmost large ones. Comparing the distributions of the latter at the two shear-rates considered, we can see that the peak is narrower in the region where the van der Waals forces dominate the behavior of the suspension (left panel), with the particles gathering in a spherical-shaped cluster. A snapshot of the structures for the case with a salt concentration of $0.4M$ is shown in Fig. 11 (left panel), where the two peaks seen in the distributions can be clearly recognized. In the right panel of Fig. 11, instead, a snapshot during the time evolution of the clusters is shown, with the large cluster fragmented in many smaller ones.

B. Wavy shear-flow

The examples discussed above show that the code is able to tackle particles suspended in a uniform shear-flow. We extend here the simulations to non-uniform shear-flows that activate the Faxén contribution introduced in the Stokes drag. In particular, we introduce a wavy shear-flow,

$$\mathbf{U}^\infty = \begin{pmatrix} \dot{\gamma}y + \mathcal{U} \sin\left(\frac{2\pi n}{L_y}y\right) \\ 0 \\ 0 \end{pmatrix}, \quad (17)$$

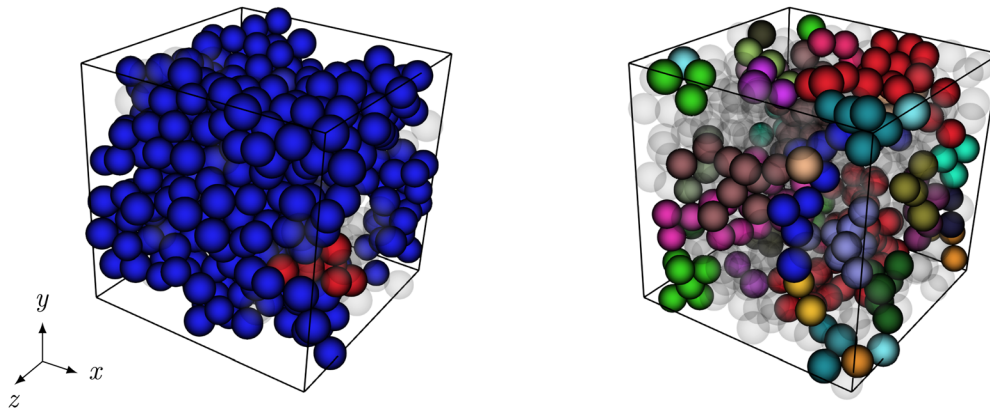


FIG. 11. Snapshot of the cluster of contacting particles at $\dot{\gamma}/\dot{\gamma}_0 = 10^{-5}$. Left panel: steady-state regime; right panel: transient regime. The total number of particles is $N = 512$. The smaller cluster plotted has a size of five particles; smaller clusters are not shown for clarity of the images.

TABLE V. Parameters set for dense suspensions in a uniform shear-flow (NW) and in a wavy one (YW), following Eq. (17). Here, $a_0 = a_1$ represents the reference length scale.

	N	a_2/a_1	V_2/V_1	St	\hat{k}	k_t/k_n	$\gamma_n \dot{\gamma}/k_n$	μ_C	$\dot{\gamma}/\dot{\gamma}_0$	δ_{hub}/a_0	λ_D/a_0	F^R/F^A	$\mathcal{U}/\dot{\gamma}a_0$	n
NW	2^{16}	3	0.25	10^{-3}	4×10^5	2/7	10^{-7}	1	1	0.25	0.02	19	0	0
YW	2^{16}	3	0.25	10^{-3}	4×10^5	2/7	10^{-7}	1	1	0.25	0.02	19	20	1

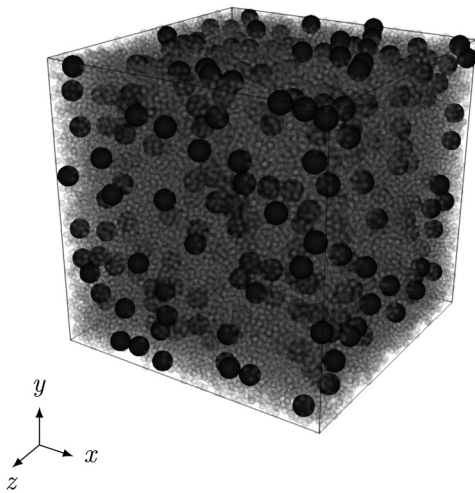


FIG. 12. Snapshot of the large domain simulation with $N = 65\,536$ and $a_2/a_1 = 3$. The volume fraction is $\phi = 0.5$, with a volume contribution of the bidispersed particles $V_2/V_1 = 0.25$.

where \mathcal{U} is the amplitude of the wave and n imposes the number of spatial periods within the domain. This is a condition of relevant interest as it can be used for example to reproduce the wall effects that appear in a rheometer when attempting to replicate a uniform shear-flows or to take into account the back-reaction of the particles on the flow itself.

We consider a cubic box containing a bidispersed suspension with volume fraction $\phi = 0.5$. The ratio between the radii of the two dispersed phases is $a_2/a_1 = 3.0$, while the volume percentage ratio of the largest dispersed particles to the smallest one is $V_2/V_1 = 0.25$. We set the number of particles to $N = 65\,536$ to test the memory-efficiency of the software. The side length of the box accommodates the volume fraction $\phi = 0.5$, being $a_0 = a_1 = 1$. The particles composing the suspension are considered to be rigid with a non-smooth surface (i.e., with a friction coefficient $\mu_C = 1$), electrically charged with a screening length $\lambda_D = 0.02a_0$. The

equivalent shear-rate, Eq. (14), is set to $\hat{\gamma} = 1$ (i.e., within the shear-thickening region of Fig. 9), with a ratio $F^R/F^A = 19$ when the pair of particles (i, j) are at contact. The wave was chosen to have a single spatial period, $n = 1$, with a large amplitude $\mathcal{U} = 20\hat{\gamma}a_0$ to amplify the effects of the wavy shear. Table V wraps up the set of parameters chosen and a snapshot of the domain and particles is shown in Fig. 12.

A wave with a large amplitude, such as the one applied in the case described above, significantly affects the local shear-rate, as shown in the left panel of Fig. 13. This local effect has a direct impact on the suspension as half of it is located in a low shear-rate region, while the other half feels a high shear-rate. Thus, the non-uniformity impacts the rheology of the suspension modifying the relative viscosity η_r of the suspension, as shown in the right of Fig. 13. Note that both cases analyzed started from an identical initial condition.

Next, in Fig. 14 we plot the shear-wise diffusivity (left panel) and the autocorrelation function of the shear-wise velocity fluctuations (right panel), respectively, defined as

$$D_y = \frac{1}{a_0^2 \hat{\gamma}} \frac{\langle [y(t) - y(t_0)]^2 \rangle}{2(t - t_0)}, \quad (18)$$

and

$$C_v = \frac{\langle v'(t)v'(t_0) \rangle}{\langle v'(t)^2 \rangle}, \quad (19)$$

where in both equations, the $\langle \rangle$ brackets indicate the average over all the particles and t_0 is the initial time; $y(t)$ and $v'(t)$ are the time-dependent shear-wise location and velocity fluctuations, respectively, of the particles. The figure shows how the particles, on average, diffuse more (twice more) when the wavy-shear rate is applied to the suspension, due to the non-uniformity of the shear rate. Moreover, the autocorrelation function of v' shows a higher integral timescale for the suspension with the non-uniform shear-rate.

Finally, to understand the temporal behavior of the suspension, we show the distribution of the local volume fraction along the shear-wise direction. Figure 15 shows the distribution of the particles in the shear-wise direction separated by the size of the suspended phase. In

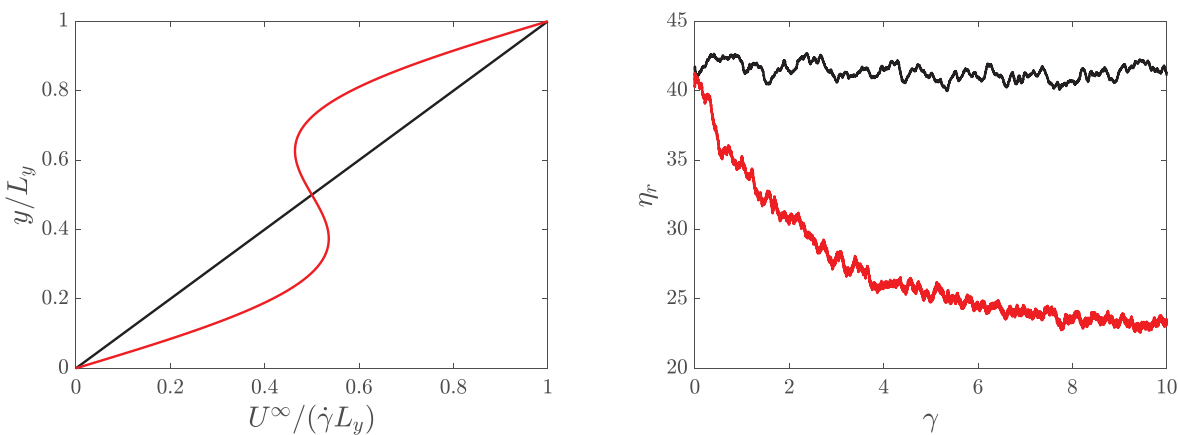


FIG. 13. Left panel: streamwise velocity profile of the carrier flow applied in the shear-wise direction, y . Right panel: time history of the relative viscosity η_r , being $\gamma = t\hat{\gamma}$ the number of strains. In both panels, the black line represents the suspension in a uniform shear-flow, while the red line the suspension in a wavy one.

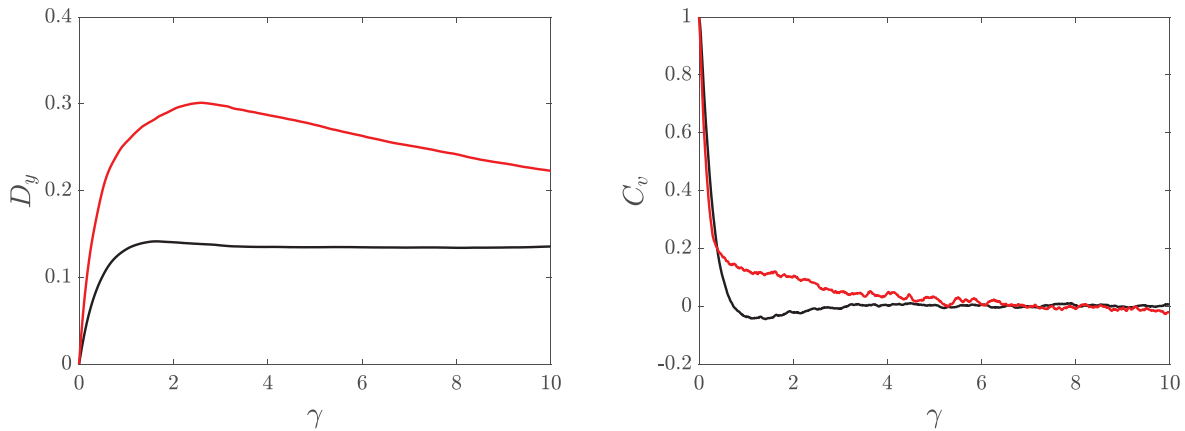


FIG. 14. Left panel: time-history of the shear-wise (y -direction) diffusivity of the particles. Right panel: time history of the autocorrelation function of the shear-wise velocity fluctuations v' . The non-dimensional time is plotted in term of strains, $\gamma = t\dot{\gamma}$. In both panels, the black line represents the suspension in a uniform shear-flow, while the red line the suspension in a wavy one.

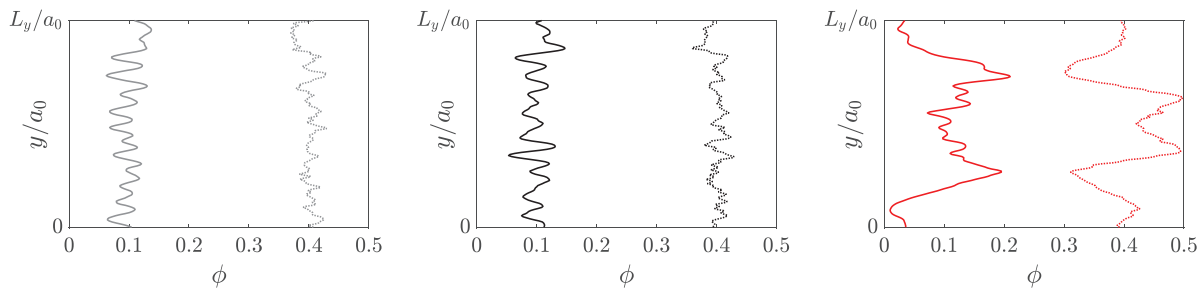


FIG. 15. Local distribution of the volume fraction along the shear-wise direction. The solid lines represent the distribution of the large particles, while the dotted lines the distribution of the small particles. Left panel: initial condition; middle panel: uniform shear-rate; right panel: wavy shear-rate. The distributions are averaged over 100 snapshots.

particular the figure is organized as follows: in the left panel, the local distributions of the large (solid line) and the small (dotted line) particles of the suspension at the initial time are shown; in the middle panel, the same quantities are shown for the particles suspended in a uniform shear-flow at $\gamma = 10$; in the right panel, the local distributions are shown for the particles suspended in a wavy shear-flow at $\gamma = 10$. While the distribution of the particles in the case where a uniform shear-rate is applied to the suspension remains similar to the initial condition with the particles uniformly distributed along the shear-wise direction, in the case where the particles are suspended in a non-uniform shear flow, two clear peaks in the distribution of the large particles appear. This suggests that the large particles are migrating toward such region that, in particular, coincide with the location of zero-shear.

IV. SUMMARY AND OUTLOOK

We have presented an efficient software (freely available at <https://github.com/marco-rosti/CFF-Ball-0x>) that tackles the dynamics of dense suspensions. First, the models of the contributions adopted to simulate the particle–particle and the particle–flow interactions have been presented. The models mimic the ones already available in the literature, echoing in particular, the implementation of Mari *et al.*²⁶ and Ge *et al.*^{29,30} The core of the algorithm, i.e., the fixed-radius

near neighbors search, follows the idea of Hoetzlein²⁵ with an improved symmetric search that guarantees a speed-up in the near neighbors inquiry and a good load-balance among processes when the parallelization is adopted. Particular attention has been also given to the memory efficiency aspect of the implementation as the representation of rheological suspension with a large number of non-smooth particles is of high interest, especially to cope with particle suspensions having a high size ratio, as a limited number of large particles would fit into small domains.

The aforementioned features of the implementation have been proved in the examples carried out in Sec. III. First, we verified the reliability of the method by comparing our results with data available in the literature obtained from other codes or experiments. Then, we carried out sample simulations with a high number of particles $N = 2^{16}$, comparing the rheology of suspensions driven by a uniform and a wavy shear-flow.

The present code can be extended in a series of ways. Models in consideration for future implementations concern the possibility of reproducing Brownian particles and the introduction of walls that constrains the particles in any of the three directions. The present code is meant to be used for studying the rheology of particle suspensions in several configurations, to unravel some of the complex phenomena arising when dealing with dense suspensions.³⁸

ACKNOWLEDGMENTS

All authors gratefully acknowledge the support of Okinawa Institute of Science and Technology Graduate University (OIST) with subsidy funding from the Cabinet Office, Government of Japan. The authors also acknowledge the computer time provided by the Scientific Computing section of Research Support Division at OIST. A. Q. S. acknowledges funding from the Joint Research Projects (JRPs) supported by JSPS and SNSF. V. R. also acknowledges financial support from the Japanese Society for the Promotion of Science (Grant No. 21K13895).

APPENDIX A: HYDRODYNAMIC RESISTANCES

The hydrodynamics of a dense suspension is dominated by contribution of the close approaching particles.¹⁵ In a Stokesian framework, this translates in dropping the full description of the flow and modeling the hydrodynamics contribution acting on the suspension with only close-range terms, described by the resistance matrices in Eq. (3).

Following the description in Mari *et al.*²⁶ and adding the Faxén laws,²⁷ the matrices for rigid spheres can be written as

$$\mathbb{R}_{Stokes,ij} = \begin{pmatrix} 6\pi\eta_0 a_i(1+a_i^2/6\nabla^2) & 0 & 0 & 0 \\ 0 & 6\pi\eta_0 a_j(1+a_j^2/6\nabla^2) & 0 & 0 \\ 0 & 0 & 8\pi\eta_0 a_i^3 & 0 \\ 0 & 0 & 0 & 8\pi\eta_0 a_j^3 \end{pmatrix}, \tag{A1}$$

$$\mathbb{R}_{Lub,ij} = \begin{pmatrix} X_{ii}^A \mathbb{N} + Y_{ii}^A \mathbb{T} & X_{ij}^A \mathbb{N} + Y_{ij}^A \mathbb{T} & Y_{ii}^B \mathbb{N}_\times & Y_{ji}^B \mathbb{N}_\times \\ & X_{jj}^A \mathbb{N} + Y_{jj}^A \mathbb{T} & Y_{ij}^B \mathbb{N}_\times & Y_{ji}^B \mathbb{N}_\times \\ \text{sym} & & Y_{ii}^C \mathbb{N}_\times & Y_{ij}^C \mathbb{N}_\times \\ & & & Y_{jj}^C \mathbb{N}_\times \end{pmatrix}, \tag{A2}$$

$$\mathbb{R}_{Lub,ij}^{(E)} = \begin{pmatrix} X_{ii}^G P_i \mathbb{I} + Y_{ii}^G Q_i & X_{ji}^G P_j \mathbb{I} + Y_{ji}^G Q_j \\ X_{ij}^G P_i \mathbb{I} + Y_{ij}^G Q_i & X_{jj}^G P_j \mathbb{I} + Y_{jj}^G Q_j \\ Y_{ii}^H & Y_{ji}^H \\ Y_{ij}^H & Y_{jj}^H \end{pmatrix}, \tag{A3}$$

where $\mathbb{N} = \mathbf{n} \otimes \mathbf{n}$ is the normal projection operator, $\mathbb{T} = \mathbb{I} - \mathbb{N}$ is the tangential projection operator (being \mathbb{I} the identity matrix), and $\mathbb{N}_\times = \mathbf{n} \times$ is the cross-product operator. The *ad hoc* defined operators, $P_i \mathbb{I}$ and Q_i , can be written as

$$P_i \mathbb{I} = \left(\mathbb{E}_i^\infty : \mathbb{N} - \frac{1}{3} \text{Tr} \mathbb{E}_i^\infty \right) \mathbb{I}, \tag{A4}$$

$$Q_i = 2\mathbb{E}_i^\infty - 2(\mathbb{E}_i^\infty : \mathbb{N}) \mathbb{I}. \tag{A5}$$

Finally, the scalar coefficients X and Y contain the diverging terms of the lubricant interactions,

$$X = g^X \frac{1}{d_{ij}^* + \varepsilon}, \quad Y = g^Y \log \frac{1}{d_{ij}^* + \varepsilon}, \tag{A6}$$

being $d_{ij}^* = 2d_{ij}/(a_i + a_j)$ the normalized particle–particle surface distance and ε is a small positive coefficient that avoids the singularity when the particles are at contact. The coefficients g^X and g^Y , instead, are defined as follows:

$$\begin{aligned} g^{X_{ii}^A}(\alpha) &= 2a_i \frac{\alpha^2}{(1+\alpha)^3}, & g^{X_{ij}^A}(\alpha) &= \alpha g^{X_{ii}^A}(\alpha^{-1}), \\ g^{X_{ij}^A}(\alpha) &= -2(a_i + a_j) \frac{\alpha^2}{(1+\alpha)^4}, & g^{X_{ji}^A}(\alpha) &= g^{X_{ij}^A}(\alpha^{-1}), \\ g^{Y_{ii}^A}(\alpha) &= \frac{4a_i \alpha(2+\alpha+2\alpha^2)}{15(1+\alpha)^3}, & g^{Y_{ij}^A}(\alpha) &= \alpha g^{Y_{ii}^A}(\alpha^{-1}), \\ g^{Y_{ij}^A}(\alpha) &= -\frac{4(a_i + a_j) \alpha(2+\alpha+2\alpha^2)}{15(1+\alpha)^4}, & g^{Y_{ji}^A}(\alpha) &= g^{Y_{ij}^A}(\alpha^{-1}), \\ g^{Y_{ii}^B}(\alpha) &= -\frac{2a_i^2 \alpha(4+\alpha)}{15(1+\alpha)^2}, & g^{Y_{ij}^B}(\alpha) &= -\alpha^2 g^{Y_{ii}^B}(\alpha^{-1}), \\ g^{Y_{ij}^B}(\alpha) &= \frac{2(a_i + a_j)^2 \alpha(4+\alpha)}{15(1+\alpha)^4}, & g^{Y_{ji}^B}(\alpha) &= -g^{Y_{ij}^B}(\alpha^{-1}), \\ g^{Y_{ii}^C}(\alpha) &= \frac{8a_i^3 \alpha}{15(1+\alpha)}, & g^{Y_{ij}^C}(\alpha) &= \alpha^3 g^{Y_{ii}^C}(\alpha^{-1}), \\ g^{Y_{ij}^C}(\alpha) &= \frac{2(a_i + a_j)^3 \alpha^2}{15(1+\alpha)^4}, & g^{Y_{ji}^C}(\alpha) &= g^{Y_{ij}^C}(\alpha^{-1}), \\ g^{X_{ii}^G}(\alpha) &= 2a_i^2 \frac{\alpha^2}{(1+\alpha)^3}, & g^{X_{ij}^G}(\alpha) &= -\alpha^2 g^{X_{ii}^G}(\alpha^{-1}), \\ g^{X_{ij}^G}(\alpha) &= -2(a_i + a_j)^2 \frac{\alpha^2}{(1+\alpha)^5}, & g^{X_{ji}^G}(\alpha) &= -g^{X_{ij}^G}(\alpha^{-1}), \\ g^{Y_{ii}^G}(\alpha) &= \frac{a_i^2 \alpha(4-\alpha+7\alpha^2)}{15(1+\alpha)^3}, & g^{Y_{ij}^G}(\alpha) &= -\alpha^2 g^{Y_{ii}^G}(\alpha^{-1}), \\ g^{Y_{ij}^G}(\alpha) &= -\frac{(a_i + a_j)^2 \alpha(4-\alpha+7\alpha^2)}{15(1+\alpha)^5}, & g^{Y_{ji}^G}(\alpha) &= -g^{Y_{ij}^G}(\alpha^{-1}), \\ g^{Y_{ii}^H}(\alpha) &= \frac{2a_i^3 \alpha(2-\alpha)}{15(1+\alpha)^2}, & g^{Y_{ij}^H}(\alpha) &= \alpha^3 g^{Y_{ii}^H}(\alpha^{-1}), \\ g^{Y_{ij}^H}(\alpha) &= \frac{(a_i + a_j)^3 \alpha^2(1+7\alpha)}{15(1+\alpha)^5}, & g^{Y_{ji}^H}(\alpha) &= g^{Y_{ij}^H}(\alpha^{-1}), \end{aligned} \tag{A7}$$

where $\alpha = a_j/a_i$ is the radii ratio.

APPENDIX B: ROLLING RESISTANCE

In this appendix, we describe the model used to introduce a rolling resistance between two contacting particles that can be included when necessary. We follow the work of Luding²⁰ and apply the same algorithm used for the frictional model,

$$\mathbf{F}_{ij}^{C,r,*} = k_r \boldsymbol{\xi}_{ij}^r, \quad (\text{B1a})$$

$$\mathbf{T}_{ij}^{C,r} = a_{ij} \mathbf{n} \times \mathbf{F}_{ij}^{C,r,*}, \quad (\text{B1b})$$

$$\mathbf{T}_{ji}^{C,r} = -\mathbf{T}_{ij}^{C,r}, \quad (\text{B1c})$$

where $a_{ij} = 2(a_i a_j)/(a_i + a_j)$ is the reduced radius. The sub- and superscript r state the rolling contribution, while the $*$ reports the nonphysical nature of the pseudo-force associated with rolling effects. In fact, $\mathbf{F}_{ij}^{C,r,*}$ passively contributes to the rhs of Eq. (1) through the rolling torque. The linear stretch $\boldsymbol{\xi}_{r,ij}$ associated with the rolling spring is computed as in Eq. (5), with the rolling velocity $\mathbf{u}_r = a_{ij}(\mathbf{n} \times \boldsymbol{\omega}_i - \mathbf{n} \times \boldsymbol{\omega}_j)$ and the rolling spring stiffness k_r (with the constraint $k_r/k_n \ll 1$) substituting the relative tangential velocity of the contact points \mathbf{u} , and the frictional spring stiffness k_f , respectively. Note that the limitation introduced by the Coulomb's law is still applied. For more details, the reader is referred to Ref. 20.

AUTHOR DECLARATIONS

Conflicts of Interest

The authors have no conflicts to disclose.

DATA AVAILABILITY

The data that support the findings of this study are available from the corresponding authors upon reasonable request.

REFERENCES

- ¹N. Takeishi, M. Rosti, Y. Imai, S. Wada, and L. Brandt, "Haemorheology in dilute, semi-dilute and dense suspensions of red blood cells," *J. Fluid Mech.* **872**, 818–848 (2019).
- ²K. Vercruyse, R. Grabowski, and R. Rickson, "Suspended sediment transport dynamics in rivers: Multi-scale drivers of temporal variation," *Earth-Sci. Rev.* **166**, 38–52 (2017).
- ³R. Eley, "Applied rheology and architectural coating performance," *J. Coat. Technol. Res.* **16**, 263–305 (2019).
- ⁴R. Tanner, "Aspects of non-colloidal suspension rheology," *Phys. Fluids* **30**, 101301 (2018).
- ⁵M. Wyart and M. Cates, "Discontinuous shear thickening without inertia in dense non-brownian suspensions," *Phys. Rev. Lett.* **112**, 098302 (2014).
- ⁶É. Guazzelli and O. Pouliquen, "Rheology of dense granular suspensions," *J. Fluid Mech.* **852**, P1 (2018).
- ⁷Y. Lee, Y. Luo, T. Bai, C. Velez, S. Brown, and N. Wagner, "Microstructure and rheology of shear-thickening colloidal suspensions with varying interparticle friction: Comparison of experiment with theory and simulation models," *Phys. Fluids* **33**, 033316 (2021).
- ⁸V. Sivadasan, E. Lorenz, A. Hoekstra, and D. Bonn, "Shear thickening of dense suspensions: The role of friction," *Phys. Fluids* **31**, 103103 (2019).
- ⁹A. Einstein, "Eine Neue Bestimmung Der Moleküldimensionen," Ph.D. thesis (ETH Zurich, 1905).
- ¹⁰G. Batchelor and J. Green, "The determination of the bulk stress in a suspension of spherical particles to order c^2 ," *J. Fluid Mech.* **56**, 401–427 (1972).
- ¹¹B. Alder and T. Wainwright, "Studies in molecular dynamics. I. General method," *J. Chem. Phys.* **31**, 459–466 (1959).
- ¹²L. Verlet, "Computer 'experiments' on classical fluids. I. Thermodynamical properties of Lennard-Jones molecules," *Phys. Rev.* **159**, 98 (1967).
- ¹³A. Sierou and J. Brady, "Accelerated Stokesian dynamics simulations," *J. Fluid Mech.* **448**, 115–146 (2001).
- ¹⁴P. Cundall and O. Strack, "A discrete numerical model for granular assemblies," *Géotechnique* **29**, 47–65 (1979).
- ¹⁵R. Ball and J. Melrose, "A simulation technique for many spheres in quasi-static motion under frame-invariant pair drag and Brownian forces," *Physica A* **247**, 444–472 (1997).
- ¹⁶R. Seto, R. Mari, J. Morris, and M. Denn, "Discontinuous shear thickening of frictional hard-sphere suspensions," *Phys. Rev. Lett.* **111**, 218301 (2013).
- ¹⁷J. Israelachvili, *Intermolecular and Surface Forces* (Academic Press, 2011).
- ¹⁸S. Li, J. Marshall, G. Liu, and Q. Yao, "Adhesive particulate flow: The discrete-element method and its application in energy and environmental engineering," *Prog. Energy Combust. Sci.* **37**, 633–668 (2011).
- ¹⁹A. Singh, S. Pednekar, J. Chun, M. Denn, and J. Morris, "From yielding to shear jamming in a cohesive frictional suspension," *Phys. Rev. Lett.* **122**, 098004 (2019).
- ²⁰S. Luding, "Cohesive, frictional powders: Contact models for tension," *Granular Matter* **10**, 235 (2008).
- ²¹A. Townsend and H. Wilson, "Frictional shear thickening in suspensions: The effect of rigid asperities," *Phys. Fluids* **29**, 121607 (2017).
- ²²Y. Guo and J. Curtis, "Discrete element method simulations for complex granular flows," *Annu. Rev. Fluid Mech.* **47**, 21–46 (2015).
- ²³J. Bentley, "Survey of techniques for fixed radius near neighbor searching," Report No. SLAC-186; STAN-CS-75-513 (Stanford Linear Accelerator Center, CA, 1975).
- ²⁴M. Howard, J. Anderson, A. Nikoubashman, S. Glotzer, and A. Panagiotopoulos, "Efficient neighbor list calculation for molecular simulation of colloidal systems using graphics processing units," *Comput. Phys. Commun.* **203**, 45–52 (2016).
- ²⁵R. Hoetzlein, "Fast fixed-radius nearest neighbors: Interactive million-particle fluids," in GPU Technology Conference (2014).
- ²⁶R. Mari, R. Seto, J. Morris, and M. Denn, "Shear thickening, frictionless and frictional rheologies in non-Brownian suspensions," *J. Rheol.* **58**, 1693–1724 (2014).
- ²⁷E. Guazzelli and J. Morris, *A Physical Introduction to Suspension Dynamics* (Cambridge University Press, 2011), Vol. 45.
- ²⁸L. Gálvez, S. de Beer, D. van der Meer, and A. Pons, "Dramatic effect of fluid chemistry on cornstarch suspensions: Linking particle interactions to macroscopic rheology," *Phys. Rev. E* **95**, 030602 (2017).
- ²⁹Z. Ge and L. Brandt, "Implementation note on a minimal hybrid lubrication/granular dynamics model for dense suspensions," arXiv:2005.12755 (2020).
- ³⁰Z. Ge, R. Martone, L. Brandt, and M. Minale, "Weakly adhesive suspension shows rate-dependence in oscillatory but not steady shear flows," arXiv:2006.04494 (2020).
- ³¹R. Groot and P. Warren, "Dissipative particle dynamics: Bridging the gap between atomistic and mesoscopic simulation," *J. Chem. Phys.* **107**, 4423–4435 (1997).
- ³²A. Lees and S. Edwards, "The computer study of transport processes under extreme conditions," *J. Phys. C* **5**, 1921 (1972).
- ³³A. Donev, "Jammed packings of hard particles," Ph.D. thesis (Princeton University, 2006).
- ³⁴O. Cheal and C. Ness, "Rheology of dense granular suspensions under extensional flow," *J. Rheol.* **62**, 501–512 (2018).
- ³⁵W. Stöber, A. Fink, and E. Bohn, "Controlled growth of monodisperse silica spheres in the micron size range," *J. Colloid Interface Sci.* **26**, 62–69 (1968).
- ³⁶L. Zhang, M. D'Acunzi, M. Kappl, G. Auernhammer, D. Vollmer, C. van Kats, and A. van Blaaderen, "Hollow silica spheres: Synthesis and mechanical properties," *Langmuir* **25**, 2711–2717 (2009).
- ³⁷V. Rathée, A. Monti, M. Rosti, and A. Shen, "Shear thickening behavior in dense repulsive and attractive suspensions of hard spheres," *Soft Matter* **17**, 8047 (2021).
- ³⁸J. Morris, "Shear thickening of concentrated suspensions: Recent developments and relation to other phenomena," *Annu. Rev. Fluid Mech.* **52**, 121–144 (2020).